

Circular THz ratchets in a 2D-modulated Dirac system

M. Hild,¹ I. Yahniuk,¹ L. E. Golub,¹ J. Amann,¹ J. Eroms,¹
D. Weiss,¹ K. Watanabe,² T. Taniguchi,³ and S. D. Ganichev¹

¹*Terahertz Center, University of Regensburg, 93040 Regensburg, Germany*

²*Research Center for Electronic and Optical Materials,
National Institute for Materials Science, 1-1 Namiki, Tsukuba 305-0044, Japan*

³*Research Center for Materials Nanoarchitectonics,
National Institute for Materials Science, 1-1 Namiki, Tsukuba 305-0044, Japan*

We report on the observation of the circular ratchet effect excited by terahertz laser radiation in a specially designed two-dimensional metamaterial consisting of a graphene monolayer deposited on a graphite gate patterned with an array of triangular antidots. We show that a periodically driven Dirac fermion system with spatial asymmetry converts the a.c. power into a d.c. current, whose direction reverses when the radiation helicity is switched. The circular ratchet effect is demonstrated for room temperature and a radiation frequency of 2.54 THz. It is shown that the ratchet current magnitude can be controllably tuned by the patterned and uniform back gate voltages. The results are analyzed in the light of the developed microscopic theory considering electronic and plasmonic mechanisms of the ratchet current formation.

I. INTRODUCTION

Single field-effect transistors (FETs) have proven to be promising devices for sensitive and fast room-temperature detection of terahertz (THz) radiation, see, e.g., [1–9]. In the last decade, it has been suggested that the performance of FET structures can be significantly improved by fabricating an asymmetric comb-like dual grating-gate (DGG) FETs based on semiconductor quantum wells or graphene [10–31]. Furthermore, it has been shown that electronic and plasmonic ratchet effects in DGG-based metamaterials lead to a helicity-driven photoresponse that reverses the sign by switching from right-handed to left-handed circular polarization [10, 13, 18, 19, 25, 28, 32, 33]. This is in contrast to the single FET in which a helicity-driven photoresponse can only be obtained due to an interference of plasma oscillations in the channel of the FETs connected to specially designed antennas [34–36], e.g., a tilted bow-tie antenna [37, 38]. Therefore, metamaterials can not only improve the performance of FET detectors, but also lead to new functionalities, in particular, the all-electric detection of radiation helicity. Thus, the search for novel concepts and designs of metamaterials that provide the helicity-sensitive dc current in response to terahertz radiation is an important and challenging task. Here, we report on the observation and study of the helicity-driven dc current excited by THz radiation in a 2D metamaterial consisting of a graphite gate patterned with an array of triangular antidots and placed under a graphene monolayer. We show that the photoresponse is due to the ratchet current caused by the combined action of a spatially periodic in-plane electrostatic potential and a periodically modulated radiation electric field caused by near-field diffraction. We investigate an all-electrically tunable magnitude of the rectified voltage that is different for clockwise and counter-clockwise circularly polarized radiation. The data are discussed in the light of the

developed theory, which is based on the solution of the Boltzmann kinetic equation and well describes all experimental findings. The results are analyzed in terms of electronic and plasmonic mechanisms of photocurrent generation in periodic structures. We show that the ratchet photocurrent arises due to the noncentrosymmetric unit cell of the periodic structure.

II. SAMPLE AND METHODS

Figures 1 (a) and (b) show the design of the investigated metamaterial. The monolayer of graphene encapsulated between hexagonal boron nitride (hBN) is deposited on the patterned bottom gate made of five layers of graphene. The pattern consists of equilateral triangular antidots arranged in a square lattice; see Fig. 1 (b). The antidots array has a period of 1000 nm. In addition, a Si wafer with a 285 nm SiO₂ layer on top was used as a uniform back gate. Two Hall bar samples with ohmic chromium-gold contacts were fabricated. The length and width of the sample A (B) were 16 μm (7.5 μm) and 2.5 μm (3.5 μm), respectively. Consequently, the area of the Hall bar structures A_s was 40 μm^2 for sample A and 26 μm^2 for sample B. The maximum charge densities for the studied patterned gate voltage V_p , ranging from -0.75 V to 0.75 V were $4 \times 10^{11} \text{ cm}^{-2}$ for electrons and $5.5 \times 10^{11} \text{ cm}^{-2}$ for holes. The maximum carrier mobility for electrons and holes are $10^4 \text{ cm}^2/\text{Vs}$ and $0.7 \times 10^4 \text{ cm}^2/\text{Vs}$, respectively. Further details on sample preparation and transport characteristics can be found in Ref. [31], where the same samples were investigated.

To excite ratchet currents, we used polarized THz radiation from a cw molecular laser optically pumped by a CO₂ laser with CH₃OH as active medium operating at frequency $f = 2.54$ THz (wavelength $\lambda = 118 \mu\text{m}$) and power at the sample position of about 30 mW. The sample

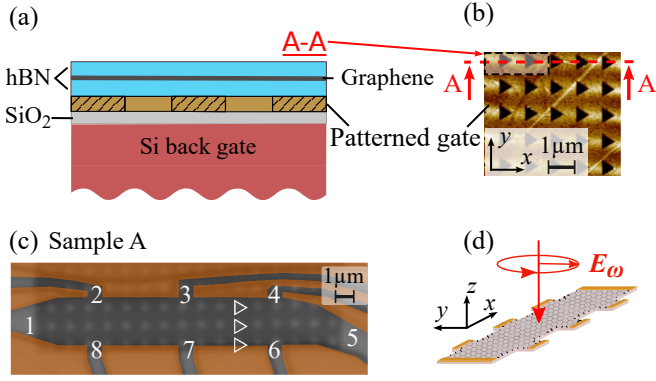


FIG. 1. Panel (a): Cross section of the two unit cells, see dashed rectangular in the panel (b). Panel b: (b) AFM image of the patterned gate formed by the periodic array of triangular antidots arranged in a square lattice. Panel (c): A photograph of sample A (the orange area is the etch mask overlay), in which triangles are highlighted by a white line and the numbers enumerate the contacts. Panel d: Experimental setup.

was excited by normally incident elliptically (circularly) polarized radiation, see Fig. 1. A Gaussian-like shape of the beam measured by a pyroelectric camera [39, 40] had a full width at half maximum of 1.8 mm and a beam area $A_{\text{beam}} \approx 0.025 \text{ cm}^2$ at the sample position. Considering the area of the Hall bar, the sample was exposed to the power $P_s = P \times A_s/A_{\text{beam}}$. The radiation polarization of the initially linearly polarized laser radiation with $\mathbf{E} \parallel y$ was obtained using crystal quartz lambda quarter plates. The plate was rotated counterclockwise by an angle φ between the x -axis and the c -axis of the plate. In this geometry, the degree of circular polarization varies according to $P_{\text{circ}} = (I^{\sigma^+} - I^{\sigma^-}) / (I^{\sigma^+} + I^{\sigma^-}) = \sin 2\varphi$. Here I^{σ^+} (I^{σ^-}) is the intensity of the right- (left-) handed circularly polarized radiation. Consequently, for $\varphi = 45^\circ$ and 135° the radiation was right-handed (σ^+) and left-handed (σ^-) circularly polarized, respectively. The polarization ellipses for some angles φ are sketched on top of Fig. 2.

The radiation was modulated by an optical chopper at a frequency 130 Hz and the photovoltage U was measured using the standard lock-in technique. The samples were placed in a vacuum chamber with a z -cut crystal quartz optical window covered with a black polyethylene foil to prevent illumination by visible and near infrared light. The voltage U_x was measured at the contacts 5-1 and U_y was measured at the contacts 8-2, with contacts 1 and 2 grounded. The generated ratchet current density was calculated as $j = U/(R_s w)$, where $R_s \ll R_{\text{in}}$ is the two-point sample resistance, R_{in} is the input impedance of the amplifier, and w is the Hall bar width. All experiments were conducted at room temperature.

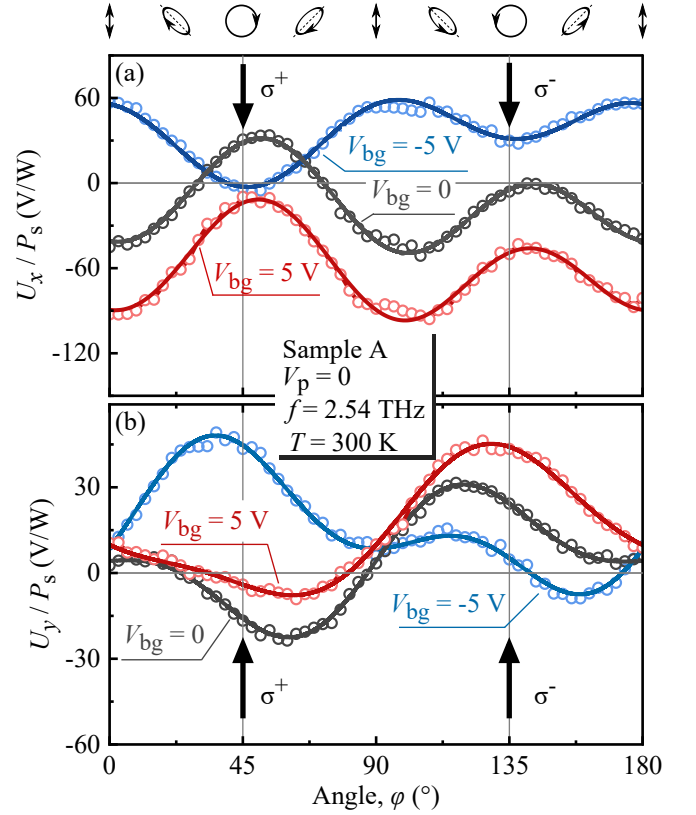


FIG. 2. Photovoltage normalized to the radiation power P_s as a function of the angle φ , which determines the radiation helicity. The data are obtained for sample A. Panels (a) and (b) show the U_x/P_s and U_y/P_s measured across the long (contacts 1-5) and short (contacts 8-2) sides of the Hall bar for different back gate voltages and for $V_p = 0$. The curves are fits according to Eq. (1) and (2) with the fitting parameters given in Tab. I. The ellipses on top illustrate the polarization states for different angles φ .

	Parameter (V/W)	V_{bg} (V)		
		-5	0	5
U_x	U^{circ}	17	-17	-25
	U_0	14	12	-31
	U_{L1}	-41	53	59
	U_{L2}	5	-28	-17
U_y	\tilde{U}^{circ}	-19	20	-1
	\tilde{U}_0	25	4	-22
	\tilde{U}_{L1}	16	0	-14
	\tilde{U}_{L2}	21	21	-3

TABLE I. Parameters used for fitting of experimental curves in Fig. 2.

III. RESULTS

When the structures were illuminated with elliptically polarized radiation, we measured a photosignal U_x from the source-drain contact pair, i.e. via the long side of the Hall bar and the signal U_y perpendicular to it from the

contact pair 8-2, Fig. 1(c). Figure 2 shows the photosignal as a function of the angle φ , which controls the radiation helicity and the degree of linear polarization. The data are presented for sample A and show that the overall polarization dependence can be well fitted by

$$j_x \propto U_x = U^{\text{circ}} \sin 2\varphi + U_0 - U_{L1} (1 + \cos 4\varphi)/2 - U_{L2} \frac{\sin 4\varphi}{2}, \quad (1)$$

$$j_y \propto U_y = \tilde{U}^{\text{circ}} \sin 2\varphi + \tilde{U}_0 - \tilde{U}_{L1} (1 + \cos 4\varphi)/2 - \tilde{U}_{L2} \frac{\sin 4\varphi}{2}. \quad (2)$$

The φ -dependent terms in Eqs. (1), (2) are the Stokes parameters describing the degrees of linear and circular polarization of the elliptically polarized radiation:

$$P_{L1} = -\frac{1 + \cos 4\varphi}{2}, \quad P_{L2} = -\frac{\sin 4\varphi}{2}, \quad P_{\text{circ}} = \sin 2\varphi. \quad (3)$$

As a central result, the figure shows that in all experimental traces obtained for different back gate voltages, the signals excited by left and right circularly polarized radiation are different in magnitude and, in some traces, of opposite sign. This is due to the significant contribution of the circular photoresponse given by the first term on the right-hand side of both equations, which describes the photocurrent proportional to the degree of the circular polarization P_{circ} . Although we obtained similar results for samples A and B, in the following, we focus on the data obtained in sample A and present the data for sample B in Appendix A.

Figure 2 and Eqs. (1), (2) show that the helicity-driven photocurrent is superimposed by the polarization-independent ratchet current given by the terms U_0 and \tilde{U}_0 and the linear ratchet current given by the terms proportional to the coefficients U_{L1} , \tilde{U}_{L1} , U_{L2} , \tilde{U}_{L2} . These contributions have been previously detected and studied using linearly polarized radiation on the same structure, see Ref. [31]. For pure circularly polarized radiation obtained at $\varphi = 45^\circ$ and 135° , P_{L1} and P_{L2} vanish. Consequently, the photosignal in response to the circularly polarized radiation is given by

$$U_x^{\text{circ}} = \pm U^{\text{circ}} + U_0, \quad U_y^{\text{circ}} = \pm \tilde{U}^{\text{circ}} + \tilde{U}_0, \quad (4)$$

where the + and - signs correspond to the right- and left-handed circularly polarized radiation respectively.

Figure 2 and the insets in Figs. 3 and 4 show that the signals in response to right- and left-handed circularly polarized radiation are sensitive to the gate voltage: they are consistently different in magnitude, and for certain gate voltages opposite in sign. To analyze the gate voltage dependencies of the helicity-driven photoresponses U^{circ} and \tilde{U}^{circ} , we used the fact that these contributions change

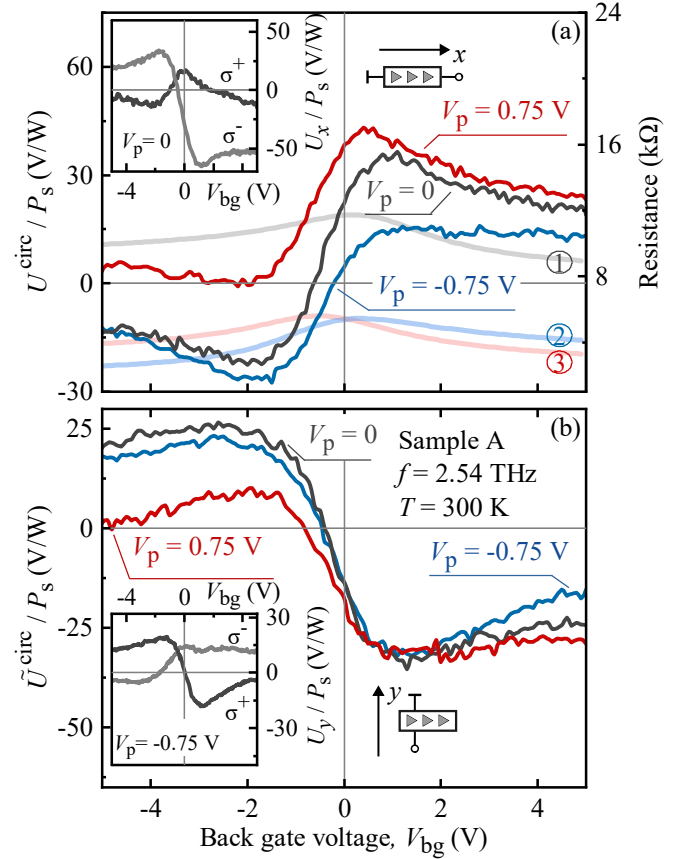


FIG. 3. Normalized photovoltages U^{circ}/P_s , panel (a) and $\tilde{U}^{\text{circ}}/P_s$, panel (b) as a function of the back gate voltage V_{bg} . The data are obtained for three values of the patterned gate voltages $V_p = 0, \pm 0.75$ V. Curves ①, ②, and ③ show back gate voltage dependencies of the two-point sample resistance (right y -axis) obtained for the patterned gate voltages $V_p = 0, -0.75, \text{ and } 0.75$ V, respectively. Insets show the back gate dependencies of the signal excited by right (σ^+) and left (σ^-) circularly polarized radiation. Insets show the Hall bar with triangular antidots and contacts used for signal detection.

sign by reversing the radiation helicity and calculated them according to $(U_{x,y}^{\sigma^+} - U_{x,y}^{\sigma^-})/2$.

The gate dependencies of the circular photosignal are shown in Figs. 3 and 4. The curves are obtained by varying one gate voltage V_{bg} or V_p and holding the other constant. Note that due to the patterned graphite gate placed between the graphene layer and the uniform back gate, a voltage applied to the latter gate is in fact not uniform and introduces an asymmetry of the electrostatic potential acting on the graphene layer. Figures 3 and 4 show that varying the asymmetric potential obtained by changing either V_{bg} or V_p changes the signal in a similar way: it increases or decreases significantly near the resistance maximum and varies only slightly at high gate voltages. At the same time, depending on the value and sign of the constant gate voltage, it may (i) change sign near the resistance maximum, see, e.g., the traces in Fig. 3(a) for $V_p = -0.75$ V or Fig. 3(b); or (ii) not change sign, see,

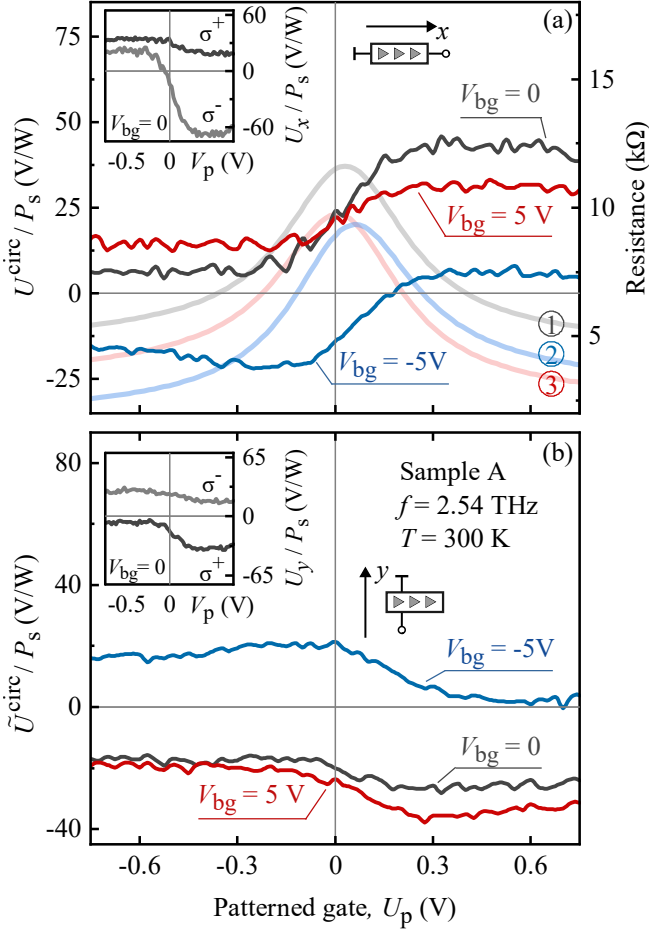


FIG. 4. Normalized photovoltages U^{circ}/P_s , panel (a), and $\tilde{U}^{\text{circ}}/P_s$, panel (b), as a function of the patterned gate voltage U_p . The data are obtained for three values of the back gate voltages $V_{\text{bg}} = 0, \pm 5$ V. Curves ①, ②, and ③ show the patterned gate voltage dependencies of the two-point sample resistance (right y -axis) obtained for the back gate voltages $V_{\text{bg}} = 0, -5$, and 5 V, respectively. Insets show the back gate dependencies of the signal excited by right (σ^+) and left (σ^-) circularly polarized radiation. Insets show the Hall bar with triangular antidots and contacts used for signal detection.

e.g., Fig. 4. A comparison of the results obtained for the source-drain contacts with those obtained for the contact pair across the Hall bar shows that the circular effect for the direction along the heights of the triangles and their bases consistently have opposite signs.

IV. THEORY

Observation of the photocurrent excited in an unbiased graphene sample using normally incident homogeneous radiation shows that the photoresponse is caused by the asymmetric patterned gate placed under the graphene layer. The asymmetric periodic array reduces the symmetry of the system allowing the generation of such a photocurrent. A previous study of the ratchet effect excited by THz radiation in the same samples demonstrated

that the system under study has C_1 point symmetry without any non-trivial symmetry elements [31]. In the theory, the ratchet current is caused by the simultaneous action of the asymmetric static potential $V(\mathbf{r})$ and the THz near-field with amplitude $E_0(\mathbf{r})$, formed by radiation diffraction at the edges of the triangular antidots. Both the potential and the near-field are 2D-periodic with the period of the structure. The low symmetry of the studied system is captured by the following vector parameter

$$\Xi_{2D} = \overline{E_0^2(\mathbf{r}) \nabla V(\mathbf{r})}, \quad (5)$$

where the overline indicates the averaging over the 2D period. Although both the near-field intensity and the periodic potential are zero on average, Ξ_{2D} is finite due to the low symmetry of the structure.

For structures with C_1 point symmetry, both Cartesian components of the vector Ξ_{2D} , Ξ_x and Ξ_y , are nonzero. This implies that the ratchet current allowed under normal light incidence in both x - and y - directions in the structure plane is:

$$j_x = -\Xi_y \gamma P_{\text{circ}} + \Xi_x (\chi_0 + \chi_1 P_{L1}) + \Xi_y \chi_2 P_{L2}, \quad (6)$$

$$j_y = \Xi_x \gamma P_{\text{circ}} + \Xi_y (\chi_0 - \chi_1 P_{L1}) + \Xi_x \chi_2 P_{L2}. \quad (7)$$

Here $j_{x,y}$ are the components of the electric current density, and the values χ_0 , $\chi_{1,2}$ and γ describe the polarization independent, linear and circular ratchet currents, respectively. The Stokes parameters of the radiation are defined by the complex polarization vector \mathbf{e} : $P_{L1} = |e_x|^2 - |e_y|^2$, $P_{L2} = e_x e_y^* + e_x^* e_y$, $P_{\text{circ}} = -i[\mathbf{e} \times \mathbf{e}^*]_z$, where we take into account that the radiation propagates along the $-z$ direction. The circular ratchet current reverses its direction when switching from σ^+ to σ^- polarization because it is proportional to the degree of circular polarization P_{circ} . For circularly polarized radiation the circular ratchet current is superimposed on the polarization-independent current, whereas for elliptically polarized light the linear ratchet effect may also contribute, see Eqs. (6), (7). As mentioned above, the theory of the polarization independent and linear ratchet currents is presented and discussed in detail in Ref. [31], so in the following, we focus on the theory of the helicity-driven ratchet current.

To develop a microscopic description of the circular ratchet current, we use the drift-diffusion approach based on the solution of the Boltzmann kinetic equation for the distribution function $f(\mathbf{p}, \mathbf{r})$

$$\frac{\partial f}{\partial t} + \mathbf{v}_p \cdot \nabla f + \mathbf{F}(\mathbf{r}, t) \cdot \frac{\partial f}{\partial \mathbf{p}} = \text{St}[f]. \quad (8)$$

Here $\mathbf{v}_p = v_0 \mathbf{p}/p$, where v_0 is the Dirac fermion velocity in graphene, St is the collision integral, and the force \mathbf{F} is a sum of the static contribution due to the potential $V(\mathbf{r})$ and a dynamic force caused by the near field:

$$\mathbf{F}(\mathbf{r}, t) = -\nabla V(\mathbf{r}) + qE_0(\mathbf{r})[\mathbf{e} \exp(-i\omega t) + c.c.], \quad (9)$$

where q is the elementary charge positive for holes and negative for electrons. By treating the periodic potential gradient and the radiation electric field as small perturbations, we iterate the kinetic Eq. (8) and find the static and homogeneous correction to the distribution function $\delta f(\mathbf{p}) \propto \Xi_{x,y}$. This allows us to calculate the ratchet current density as follows:

$$\mathbf{j} = 4q \sum_{\mathbf{p}} \mathbf{v}_{\mathbf{p}} \delta f(\mathbf{p}). \quad (10)$$

Remarkably, since we take into account either $\nabla_x V$ or $\nabla_y V$, the final expression for \mathbf{j} coincides with the result for the 1D modulation with a potential that depends only x or y . Therefore, the 2D character of the modulation is accounted for by the lateral asymmetry parameter Ξ_{2D} , while the factor γ in Eqs. (6), (7) is determined only by the properties of the 2D carriers in graphene above the periodic gate. This problem for $\Xi_{2D} \parallel x$ has already been considered for graphene in Ref. [13]. Generalizing to the case of 2D modulation with $\Xi_x \neq 0$ and $\Xi_y \neq 0$ yields, in agreement with the phenomenological Eqs. (6) and (7), the following expression for the circular ratchet current density

$$j_x^{\text{circ}} = -\Xi_y \gamma P_{\text{circ}}, \quad j_y^{\text{circ}} = \Xi_x \gamma P_{\text{circ}}, \quad (11)$$

where

$$\gamma = \frac{q^3 v_0^4 \tau_{\text{tr}}^3 \omega^2 \mathcal{F}(\omega \tau_{\text{tr}})}{2s^2 \pi \hbar^2 \varepsilon_{\text{F}} [1 + (\omega \tau_{\text{tr}})^2] [\omega^2 + (\omega^2 - \omega_{\text{pl}}^2)^2 \tau_{\text{tr}}^2]}. \quad (12)$$

Here, ε_{F} is the Fermi energy, ω is the radiation frequency, and τ_{tr} is the transport relaxation time. We take here into account a resonant enhancement of the near-field at the plasmon frequency $\omega = \omega_{\text{pl}}$ [25, 33]. In the studied 2D square lattice with the period d , we have $\omega_{\text{pl}} = s \sqrt{q_x^2 + q_y^2}$, where $q_x = q_y = 2\pi/d$, and s is the plasmon velocity.

The frequency dependence of the ratchet current varies strongly with the type of the elastic scattering potential of the carriers in graphene [13]. This is captured in Eq. (12) by the dimensionless factor $\mathcal{F}(\Omega)$ where $\Omega = \omega \tau_{\text{tr}}$. For the short-range (SR) and long-range Coulomb (Coul) scattering potentials it is given by

$$\mathcal{F}_{\text{SR}}(\Omega) = -\frac{\Omega(2\Omega^4 + \Omega^2 + 8)}{(\Omega^2 + 4)^2}, \quad \mathcal{F}_{\text{Coul}}(\Omega) = \frac{1}{\Omega}. \quad (13)$$

The divergence at $\Omega \rightarrow 0$ that appears in $\mathcal{F}_{\text{Coul}}$ is smeared by plasmon or energy relaxation processes [13]. Therefore, in calculations at $\omega_{\text{pl}} = 0$ we take $\mathcal{F}_{\text{Coul}} = \Omega / [\Omega^2 + (\tau_{\text{tr}}/\tau_{\varepsilon})^2]$, where $\tau_{\varepsilon} \gg \tau_{\text{tr}}$ is the energy relaxation time. The frequency dependence of the amplitude of the circular ratchet current generated, e.g., in y -direction $j_y^{\text{circ}} = \Xi_x \gamma$ normalized to $j_0 = \Xi_x q^3 v_0^4 \tau_{\text{tr}}^3 / (4s^2 \pi \hbar^2 \varepsilon_{\text{F}})$ is shown in Fig. 5 for two considered types of elastic scattering potentials. For Coulomb impurity scattering at $\omega_{\text{pl}} = 0$ we take $(\tau_{\text{tr}}/\tau_{\varepsilon})^2 = 0.2$.

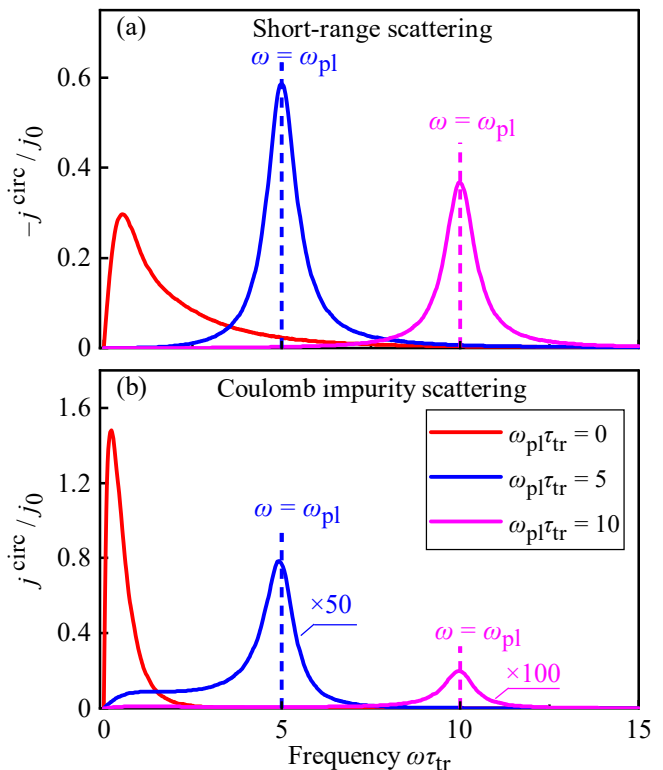


FIG. 5. Frequency dependence of the circular ratchet current for two types of elastic scattering. The curves are calculated for $\omega_{\text{pl}} = 0$ (red) and for $\omega_{\text{pl}} \tau_{\text{tr}} \gg 1$, see vertical dashed lines.

V. DISCUSSION

Now, we discuss the obtained experimental results the light of the developed theory. We begin with the polarization dependence of the observed photoresponse. As discussed in Sec. III, all curves obtained for different combinations of the gate voltages are well described by Eqs. (1) and (2), see Fig. 2. Comparing these equations with the theoretically obtained Eqs. (6), (7) for the ratchet current and noting that the Stokes parameters in our experiments vary according to Eq. (3), we see that both sets of equations represent identical dependencies on the angle φ . The three last terms in each equation with the parameters $U_0 \propto \Xi_x \chi_0$, $U_{L1} \propto \Xi_x \chi_1$, $U_{L2} \propto \Xi_y \chi_2$, $\tilde{U}_0 \propto \Xi_x \chi_0$, $\tilde{U}_{L1} \propto \Xi_y \chi_1$, and $\tilde{U}_{L2} \propto \Xi_x \chi_2$ represent the polarization independent and linear ratchet effects, which are discussed in a separate publication [31]. Here, we focus on the helicity-sensitive contribution defined by the parameters $U^{\text{circ}} \propto \Xi_y \gamma$ and $\tilde{U}^{\text{circ}} \propto -\Xi_x \gamma$. Equations (11), obtained from both the symmetry arguments and the microscopic theory, show that the circular ratchet currents excited in x - and y -direction have opposite directions provided that Ξ_x and Ξ_y have the same sign. This is in agreement with the experimental data showing that the corresponding signals have opposite signs, see e.g. Fig. 2 and insets in Figs. 3 and 4.

A fingerprint of the ratchet effects is that it is propor-

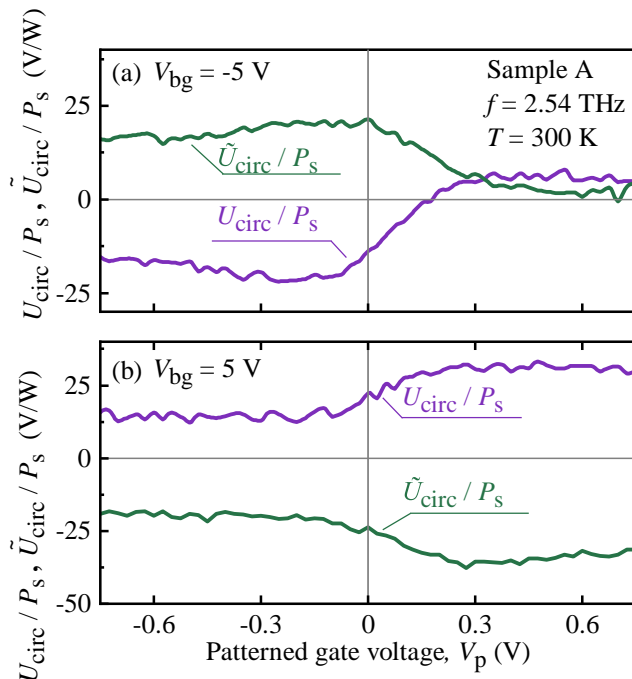


FIG. 6. Gate voltage dependencies of the normalized circular photocurrent density $j^{\text{circ}}/P_s = U^{\text{circ}}/(R_s w P_s)$ measured in the direction along the height of triangles (contacts 1-5). Curves ①, ②, and ③ in panel (a) show the back gate voltage dependencies of the two-point sample resistance (right y -axis) obtained for the patterned gate voltages $V_p = 0, -0.75,$ and 0.75 V, respectively. Curves ①, ②, and ③ in panel (b) show the patterned gate voltage dependencies of the two-point sample resistance (right y -axis) obtained for the back gate gate voltages $V_{bg} = 0, -5,$ and 5 V, respectively.

tional to the lateral asymmetry parameters Ξ_x and Ξ_y , see Eqs. (5) and (11). These parameters are defined, on the one hand, by the near field, and, on the other hand, by the asymmetry of the electrostatic potential, which can be varied by the gate voltages applied to the back and patterned gates. The simulation performed in Ref. [31] shows that both, patterned and back gate voltages, introduce an asymmetric electrostatic potential acting on the electron gas in graphene. Varying the gate voltage from negative to positive values changes the magnitude and the sign of the asymmetry. Note that even for zero potential at both gates, an asymmetry is created by the built-in potential caused by the conducting patterned gate deposited under the graphene. The calculations show that the asymmetry along the x -direction is indeed present and can be reversed by reversing the polarity of one of the gates. In particular, in the discussed metamaterial the uniform bottom gate potential leads to a change of ∇V and thus of the lateral asymmetry parameter. This is because the applied back gate voltage is periodically screened by the graphite gate. It can even lead to the formation of lateral $p-n$ junctions.

Figures 3 and 4 show that in the range of V_{bg} from -2 to 2 V and V_p from 0.1 to 0.3 V the signal measured across

the long (short) side of the Hall bar increases (decreases) linearly with the gate voltages. At higher $|V_{bg}|$ and $|V_p|$ the signal saturates or even slightly decreases, see Figs. 3 and 4. The behavior of the ratchet current calculated according to $j = U/(R_s w)$ is slightly different. This is due to the reduction of the sample resistance with respect to its value at zero gate voltages, see curves ①, ②, and ③ in Fig. 3(a) and Fig. 4(a), which affects the gate voltage dependence of the current, especially at high gate voltages. The gate dependence of the photocurrent is shown in Fig. 6, which demonstrates that its behavior only slightly differs from that of the photovoltage: in most cases it saturates at high gate voltages.

Now, we comment the sign of the photocurrent. At first glance, one could expect, since the asymmetry of the electrostatic potential reverses its sign near zero gate voltages, the current should also reverse its direction. However, the real situation is more complex. Equation (12) shows that the current is proportional to the third power of the carriers' charge; thus, varying the gate voltage may also cause the sign of the current to change. Consequently, the reversing of the sign of the electrostatic potential does not necessarily reverse the ratchet current direction. This is indeed observed in the experiment, which shows that for some values of one fixed gate voltage, the variation of the other changes the current sign, while for some values of the fixed gate the current can keep its direction, see Figs. 3(a) and Fig. 4. Such a behavior is specific to the used design of our 2D metamaterial, where the patterned gate is placed between the graphene layer and the uniform back gate. Because of the triangular antidots, both gates change the carrier density and the carrier sign inhomogeneously, either in the area outside the antidots (n, p controlled by V_p) or above the antidots (n^*, p^* controlled by V_{bg}), the 2D map of the sample resistance showing the gate voltage regions with dominating n, p, n^*, p^* carrier types is presented in Ref. [31]. By the same arguments, the lateral asymmetry parameters in these two regions, Ξ_{2D} and Ξ_{2D}^* , can also be different in magnitude and even in sign. Since the sign of the ratchet current is defined by the product $q^3 \Xi_{x,y}$ and/or $q^{*3} \Xi_{x,y}^*$, if both q and Ξ_{2D} change sign, then the direction of the ratchet current remains unchanged. Otherwise, if one of the signs holds and the other reverses, then the current direction changes.

Finally, we discuss the frequency dependence of the circular ratchet current, which was obtained theoretically, see Eqs. (11), (12) and Fig. 5, but has not been studied experimentally so far. The figure shows that the behavior of the circular ratchet current depends strongly on the value of $\omega_{pl} \tau_{tr}$. This is caused by different mechanisms of the ratchet current formation, electronic and plasmonic, realized in the limits $\omega_{pl} \tau_{tr} \ll 1$ and $\omega_{pl} \tau_{tr} \gg 1$, respectively. The frequency dependence for the first case is shown by the red curves in Fig. 5. It can be seen that the circular ratchet current behaves non-monotonically with

frequency for both types of scattering potentials and has a maximum at $\omega\tau_{\text{tr}} \lesssim 1$. This behavior is characteristic for all circular photocurrents caused by the photogalvanic effect, the dynamic Hall effect, and edge photocurrents, for reviews see [41, 42], and has the same physical background. At zero frequency, the circular polarization is absent, and subsequently circular photocurrents disappear. At finite frequency, model considerations show that a retardation of carrier motion with respect to the radiating electric field is crucial for the formation of helicity-driven photocurrents. The retardation is caused by carrier scattering, and the circular photocurrent approaches maximum at $\omega\tau_{\text{tr}} \lesssim 1$ for both types of scattering, in particular at $\omega\tau_{\text{tr}} \approx 1$ for Coulomb impurity scattering. At higher frequencies, the current decreases rapidly. Depending on the scattering potential, the asymptote at $\omega\tau_{\text{tr}} \gg 1$ is $\propto 1/\omega^3$ for short-range scattering but a much faster decrease $\propto 1/\omega^5$ is realized for long-range Coulomb impurities.

Increasing the plasmon frequency leads to the plasmonic ratchet effect, which drastically changes the frequency dependence of the circular ratchet current, see blue and magenta curves in Fig. 5 obtained for different values of $\omega_{\text{pl}} > 1/\tau_{\text{tr}}$. For both scattering potentials, in common is that the maximum of the circular ratchet current shifts to frequencies close to ω_{pl} . The width of the plasmon resonance is controlled by the quality factor given by $\omega_{\text{pl}}\tau_{\text{tr}}$. For short-range scattering, the amplitude of the current at the resonance is comparable for different values of ω_{pl} . In sharp contrast, for the Coulomb impurity scattering, an increase of ω_{pl} results in a drastic decrease of the current amplitude at resonance [43]. Therefore, it is important to know which type of scattering potential is responsible for the ratchet current. The fact that the direction of the current is opposite for two types of scattering potentials may be helpful in judging this, see Fig. 5.

To conclude the discussion on the frequency dependence of the circular ratchet current, we emphasize that the plasmonic ratchet effect for short-range scattering [44] allows for designing a helicity-sensitive photodetector for the frequency range on demand, because the plasma frequency can be tuned in a wide range by the period of the periodic array.

VI. SUMMARY

In summary, experimental results and developed theory show that excitation of graphene-based 2D metamaterials by circularly polarized THz radiation results in the helicity sensitive ratchet current. In this proof-of-principle work, the circular ratchet current is demonstrated for devices at room temperature and radiation frequency of 2.54 THz. At the same time, the developed theory and previous work on ratchet currents in 1D graphene-based metamaterials [25, 29] guarantee that such structures should also be efficient over a wide range of temperatures and frequencies.

Consequently, the proposed design of the metamaterial can be considered as a perspective for the development of novel wide-band room-temperature THz detection. As a prospect, the results of the developed theory show that metamaterials with different lattice period and cell size, characterized by different plasmon frequencies, can be used for the development of resonant helicity-sensitive terahertz detectors with the desired central frequency and enhanced responsivity.

VII. ACKNOWLEDGMENTS

We acknowledge the financial support of the Deutsche Forschungsgemeinschaft (DFG, German Research Foundation) via Project-ID 448955585 (Ga501/18), Project-ID 314695032 – SFB 1277 (Subproject A09), Project-ID 426094608 (ER 612/2-1), and of the Volkswagen Stiftung Program (97738). K.W. and T.T. acknowledge support from the JSPS KAKENHI (Grant Numbers 20H00354 and 23H02052) and World Premier International Research Center Initiative (WPI), MEXT, Japan.

Appendix A: Results obtained on sample B

Here we present the data obtained on the sample B, for its design and structure see the inset in Fig. A.1 and Sec. II. Figure A.1 show the variation of the photosignal magnitude with the angle φ' . Alike in the sample A we obtain substantial contribution of the helicity sensitive photoresponse.

The overall polarization dependence can be well fitted by

$$j_x \propto U_x = U^{\text{circ}} \sin 2\varphi' + U_0 + U_{L1} (1 + \cos 4\varphi')/2 + U_{L2} \frac{\sin 4\varphi'}{2}, \quad (\text{A1})$$

Note that, due to technical reasons in our measurements on sample B, we had to change the definition of the angle φ : the linear polarization of the laser light was oriented along the x -axis, and the angle φ' was counted from the y -direction. This resulted in the change the Stokes parameters of the contributions proportional to the coefficients U_{L1} and U_{L2} but didn't affect the contributions U^{circ} and U_0 . Consequently, for equation for the photoresponse excited by circularly polarized radiation Eq. (??) remains unchanged. The inset in Fig. A.2 and the main panel of Fig. A.2 show the back gate dependencies of the signal in response to the right- and left-handed circularly polarized radiation (inset) and of the circular and polarization-independent photoresponses (main panel). It is seen that U^{circ} varies monotonically upon increase of the gate voltage and changes its sign close to the resistance maximum. More complex gate dependence of the polarization independent part is discussed in Ref. [31].

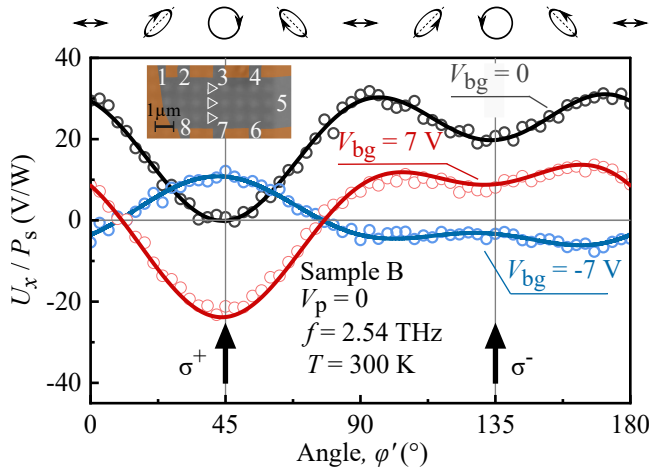


FIG. A.1. Normalized photovoltage U_x/P_s measured in sample B (contacts 1-5) as a function of the angle φ , which determines the radiation helicity. The data are obtained for three values of the back gate voltage V_{bg} holding patterned gate at zero bias. Curves are fits after Eq. (A1) with fitting parameters given in Tab. II. The inset shows a photograph of sample B (the orange area is the etching mask overlay). Note that, in contrast to the measurements performed on sample A the Hall bar is oriented vertically, i.e. at zero angle φ the radiation electric field is parallel to the x -axis. The ellipses on top illustrate the states of polarization for various angles φ .

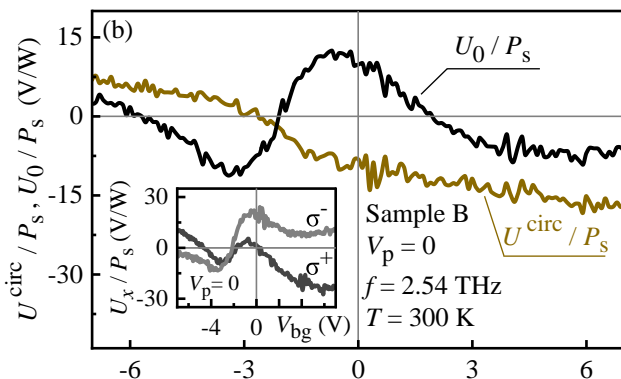


FIG. A.2. Back gate voltage dependence of the circular U_{circ} and polarization independent U_0 photosignals. The inset shows the back gate dependence of the photovoltages excited by right- and left-handed circularly polarized radiation.

Parameter (V/W)	V_{bg} (V)		
	-7	0	7
U_x			
U^{circ}	7	-10	-16
U_0	4	10	-7
U_{L1}	-7	19.5	16
U_{L2}	4	2	2

TABLE II. Parameters used for fitting of experimental curves in Fig. A.1.

[1] W. Knap, M. Dyakonov, D. Coquillat, F. Teppe, N. Dyakonova, J. Lusakowski, K. Karpierz, M. Sakowicz, G. Valusis, D. Seliuta, I. Kasalynas, A. Fatimy, Y. M. Meziani, and T. Otsuji, Field effect transistors for terahertz detection: Physics and first imaging applications, *Journal of Infrared, Millimeter, and Terahertz Waves* **10.1007/s10762-009-9564-9** (2009).
 [2] A. Lisauskas, U. Pfeiffer, E. Öjefors, P. H. Bolivar, D. Glaab, and H. G. Roskos, Rational design of high-responsivity detectors of terahertz radiation based on distributed self-mixing in silicon field-effect transistors, *Journal of Applied Physics* **105**, 10.1063/1.3140611 (2009).
 [3] L. Vicarelli, M. S. Vitiello, D. Coquillat, A. Lombardo,

A. C. Ferrari, W. Knap, M. Polini, V. Pellegrini, and A. Tredicucci, Graphene field-effect transistors as room-temperature terahertz detectors, *Nat. Mater.* **11**, 865 (2012).
 [4] F. H. L. Koppens, T. Mueller, P. Avouris, A. C. Ferrari, M. S. Vitiello, and M. Polini, Photodetectors based on graphene, other two-dimensional materials and hybrid systems, *Nat. Nanotechnol.* **9**, 780 (2014).
 [5] T. Otsuji, Trends in the research of modern terahertz detectors: Plasmon detectors, *IEEE Transactions on Terahertz Science and Technology* **5**, 1110 (2015).
 [6] J. Marczewski, D. Coquillat, W. Knap, C. Kolacinski, P. Kopyt, K. Kucharski, J. Lusakowski, D. Obrebski, D. Tomaszewski, D. Yavorskiy, P. Zagrajek, R. Ryniec, and N. Palka, Thz detectors based on si-cmos technology field effect transistors – advantages, limitations and perspectives for thz imaging and spectroscopy, *Opto-Electronics Review* **26**, 261 (2018).
 [7] D. A. Bandurin, I. Gayduchenko, Y. Cao, M. Moskotin, A. Principi, I. V. Grigorieva, G. Goltsman, G. Fedorov, and D. Svintsov, Dual origin of room temperature sub-terahertz photoresponse in graphene field effect transistors, *Appl. Phys. Lett.* **112**, 141101 (2018).
 [8] A. Rogalski, M. Kopytko, and P. Martyniuk, Two-dimensional infrared and terahertz detectors: Outlook and status, *Appl. Phys. Rev.* **6**, 021316 (2019).
 [9] R. A. Lewis, A review of terahertz detectors, *Journal of Physics D: Applied Physics* **52**, 433001 (2019).
 [10] P. Olbrich, E. L. Ivchenko, R. Ravash, T. Feil, S. D. Danilov, J. Allerdings, D. Weiss, D. Schuh, W. Wegscheider, and S. D. Ganichev, Ratchet effects induced by terahertz radiation in heterostructures with a lateral periodic potential, *Phys. Rev. Lett.* **103**, 090603 (2009).
 [11] P. Olbrich, J. Karch, E. L. Ivchenko, J. Kamann, B. März, M. Fehrenbacher, D. Weiss, and S. D. Ganichev, Classical ratchet effects in heterostructures with a lateral periodic potential, *Phys. Rev. B* **83**, 165320 (2011).
 [12] Y. Y. Kiselev and L. E. Golub, Optical and photogalvanic properties of graphene superlattices formed by periodic strain, *Phys. Rev. B* **84**, 235440 (2011).
 [13] A. V. Nalitov, L. E. Golub, and E. L. Ivchenko, Ratchet effects in two-dimensional systems with a lateral periodic potential, *Phys. Rev. B* **86**, 115301 (2012).
 [14] T. Otsuji, T. Watanabe, S. A. B. Tombet, A. Satou, W. M. Knap, V. V. Popov, M. Ryzhii, and V. Ryzhii, Emission and detection of terahertz radiation using two-dimensional electrons in III-v semiconductors and graphene, *IEEE Trans. Terahertz Sci. Technol.* **3**, 63 (2013).
 [15] C. Drexler, S. A. Tarasenko, P. Olbrich, J. Karch, M. Hirmer, F. Müller, M. Gmitra, J. Fabian, R. Yakimova, S. Lara-Avila, S. Kubatkin, M. Wang, R. Vajtai, P. M. Ajayan, J. Kono, and S. D. Ganichev, Magnetic

- quantum ratchet effect in graphene, *Nat. Nanotechnol.* **8**, 104 (2013).
- [16] Y. Kurita, G. Ducournau, D. Coquillat, A. Satou, K. Kobayashi, S. B. Tombet, Y. M. Meziani, V. V. Popov, W. Knap, T. Suemitsu, and T. Otsuji, Ultrahigh sensitive sub-terahertz detection by InP-based asymmetric dual-grating-gate high-electron-mobility transistors and their broadband characteristics, *Appl. Phys. Lett.* **104**, 251114 (2014).
- [17] G. V. Budkin and L. E. Golub, Orbital magnetic ratchet effect, *Phys. Rev. B* **90**, 125316 (2014).
- [18] P. Faltermeier, P. Olbrich, W. Probst, L. Schell, T. Watanabe, S. A. Boubanga-Tombet, T. Otsuji, and S. D. Ganichev, Helicity sensitive terahertz radiation detection by dual-grating-gate high electron mobility transistors, *J. Appl. Phys.* **118**, 084301 (2015).
- [19] P. Olbrich, J. Kamann, M. König, J. Munzert, L. Tutsch, J. Eroms, D. Weiss, M.-H. Liu, L. E. Golub, E. L. Ivchenko, V. V. Popov, D. V. Fateev, K. V. Mashinsky, F. Fromm, T. Seyller, and S. D. Ganichev, Terahertz ratchet effects in graphene with a lateral superlattice, *Phys. Rev. B* **93**, 075422 (2016).
- [20] V. V. Popov, Polarization-dependent plasmonic photocurrents in two-dimensional electron systems, *Appl. Phys. Lett.* **108**, 261104 (2016).
- [21] D. V. Fateev, K. V. Mashinsky, J. D. Sun, and V. V. Popov, Enhanced plasmonic rectification of terahertz radiation in spatially periodic graphene structures towards the charge neutrality point, *Solid-State Electron.* **157**, 20 (2019).
- [22] S. Hubmann, V. V. Bel'kov, L. E. Golub, V. Y. Kachorovskii, M. Drienovsky, J. Eroms, D. Weiss, and S. D. Ganichev, Giant ratchet magneto-photocurrent in graphene lateral superlattices, *Phys. Rev. Research* **2**, 033186 (2020).
- [23] S. Boubanga-Tombet, W. Knap, D. Yadav, A. Satou, D. B. But, V. V. Popov, I. V. Gorbenko, V. Kachorovskii, and T. Otsuji, Room-temperature amplification of terahertz radiation by grating-gate graphene structures, *Phys. Rev. X* **10**, 031004 (2020).
- [24] J. A. Delgado-Notario, V. Clericó, E. Diez, J. E. Velázquez-Pérez, T. Taniguchi, K. Watanabe, T. Otsuji, and Y. M. Meziani, Asymmetric dual-grating gates graphene FET for detection of terahertz radiations, *APL Photonics* **5**, 066102 (2020).
- [25] E. Mönch, S. O. Potashin, K. Lindner, I. Yahniuk, L. E. Golub, V. Y. Kachorovskii, V. V. Bel'kov, R. Huber, K. Watanabe, T. Taniguchi, J. Eroms, D. Weiss, and S. D. Ganichev, Ratchet effect in spatially modulated bilayer graphene: Signature of hydrodynamic transport, *Phys. Rev. B* **105**, 045404 (2022).
- [26] I. Yahniuk, G. V. Budkin, A. Kazakov, M. Otteneder, J. Ziegler, D. Weiss, N. N. Mikhailov, S. A. Dvoret'skii, T. Wojciechowski, V. V. Bel'kov, W. Knap, and S. D. Ganichev, Terahertz ratchet effect in interdigitated hgte structures, *Physical Review Applied* **18**, 054011 (2022).
- [27] K. Tamura, C. Tang, D. Ogiura, K. Suwa, H. Fukidome, Y. Takida, H. Minamide, T. Suemitsu, T. Otsuji, and A. Satou, Fast and sensitive terahertz detection in a current-driven epitaxial-graphene asymmetric dual-grating-gate fet structure 10.48550/ARXIV.2207.00135 (2022).
- [28] E. Mönch, S. O. Potashin, K. Lindner, I. Yahniuk, L. E. Golub, V. Y. Kachorovskii, V. V. Bel'kov, R. Huber, K. Watanabe, T. Taniguchi, J. Eroms, D. Weiss, and S. D. Ganichev, Cyclotron and magnetoplasmon resonances in bilayer graphene ratchets, *Physical Review B* **107**, 115408 (2023).
- [29] E. Mönch, S. Hubmann, I. Yahniuk, S. Schweiss, V. V. Bel'kov, L. E. Golub, R. Huber, J. Eroms, K. Watanabe, T. Taniguchi, D. Weiss, and S. D. Ganichev, Nonlinear intensity dependence of ratchet currents induced by terahertz laser radiation in bilayer graphene with asymmetric periodic grating gates, *Journal of Applied Physics* **134**, 10.1063/5.0165248 (2023).
- [30] E. Abidi, A. Khan, J. A. Delgado-Notario, V. Clericó, J. Calvo-Gallego, T. Taniguchi, K. Watanabe, T. Otsuji, J. E. Velázquez, and Y. M. Meziani, Terahertz detection by asymmetric dual grating gate bilayer graphene fet's with integrated bowtie antenna, *Nanomaterials* **14**, 383 (2024).
- [31] I. Yahniuk, M. Hild, L. E. Golub, J. Amann, J. Eroms, D. Weiss, W.-H. Kang, M.-H. Liu, K. Watanabe, T. Taniguchi, and S. D. Ganichev, Terahertz ratchet in graphene 2d metamaterial formed by a patterned gate with an antidot arrayd, (2024), arXiv:2402.03956 [cond-mat.mes-hall].
- [32] E. L. Ivchenko and S. D. Ganichev, Ratchet effects in quantum wells with a lateral superlattice, *JETP Lett.* **93**, 673 (2011), [Pisma v ZhETF **93**, 752 (2011)].
- [33] I. Rozhansky, V. Kachorovskii, and M. Shur, Helicity-driven ratchet effect enhanced by plasmons, *Phys. Rev. Lett.* **114**, 246601 (2015).
- [34] C. Drexler, N. Dyakonova, P. Olbrich, J. Karch, M. Schafberger, K. Karpierz, Y. Mityagin, M. B. Lifshits, F. Teppe, O. Klimenko, Y. M. Meziani, W. Knap, and S. D. Ganichev, Helicity sensitive terahertz radiation detection by field effect transistors, *J. Appl. Phys.* **111**, 124504 (2012).
- [35] K. Romanov and M. Dyakonov, Theory of helicity-sensitive terahertz radiation detection by field effect transistors, *Applied Physics Letters* **102** (2013).
- [36] I. V. Gorbenko, V. Y. Kachorovskii, and M. S. Shur, Plasmonic helicity-driven detector of terahertz radiation, *physica status solidi (RRL) – Rapid Research Letters* **13**, 10.1002/pssr.201800464 (2018).
- [37] Y. Matyushkin, S. Danilov, M. Moskotin, V. Belosevich, N. Kaurova, M. Rybin, E. D. Obraztsova, G. Fedorov, I. Gorbenko, V. Kachorovskii, and S. Ganichev, Helicity-sensitive plasmonic terahertz interferometer, *Nano Letters* **20**, 7296 (2020).
- [38] Y. Matyushkin, S. Danilov, M. Moskotin, G. Fedorov, A. Bochin, I. Gorbenko, V. Kachorovskii, and S. Ganichev, Carbon nanotubes for polarization sensitive terahertz plasmonic interferometry, *Optics Express* **29**, 37189 (2021).
- [39] S. D. Ganichev, Tunnel ionization of deep impurities in semiconductors induced by terahertz electric fields, *Phys. B* **273-274**, 737 (1999).
- [40] T. Herrmann, I. A. Dmitriev, D. A. Kozlov, M. Schneider, B. Jentzsch, Z. D. Kvon, P. Olbrich, V. V. Bel'kov, A. Bayer, D. Schuh, D. Bougeard, T. Kuczmik, M. Oltcher, D. Weiss, and S. D. Ganichev, Analog of microwave-induced resistance oscillations induced in GaAs heterostructures by terahertz radiation, *Phys. Rev. B* **94**, 081301 (2016).
- [41] M. M. Glazov and S. D. Ganichev, High frequency electric field induced nonlinear effects in graphene, *Phys. Rep.* **535**, 101 (2014).

- [42] S. D. Ganichev, D. Weiss, and J. Eroms, Terahertz electric field driven electric currents and ratchet effects in graphene, *Ann. Phys.* **529**, 1600406 (2017).
- [43] Note that in the consideration above we do not take into account effects of inter-particle scattering assuming the corresponding characteristic time is longer than the transport relaxation time due to elastic scattering τ_{tr} . In the opposite case of strong carrier-carrier scattering, the hydrodynamic regime is realized, where the behavior of the circular ratchet current at high frequencies changes substantially [25].
- [44] It is usually realized in small-sized graphene samples.